

# Aqueous Stability of Metallic Materials and Metal Oxides

Yizhan Zhang,<sup>†</sup> Lin Wang,<sup>†</sup> Elena Scivally, Kayla James, Evelyn McBride, Mahesh Dheerasinghe, Michael Shatruk, Yan Zeng,\* and Bin Ouyang\*

Cite This: <https://doi.org/10.1021/acs.chemmater.5c00455>

Read Online

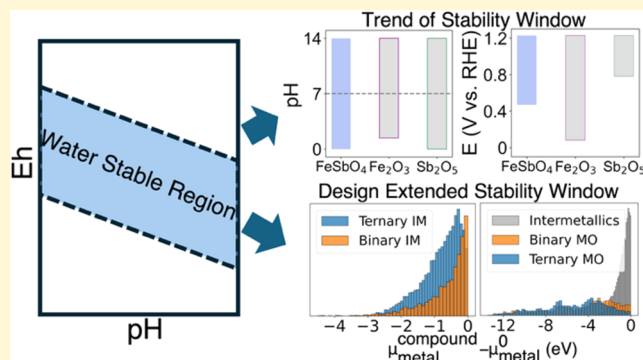
ACCESS |

Metrics & More

Article Recommendations

Supporting Information

**ABSTRACT:** Given water's ubiquity as a solvent, understanding the stability of materials in water is crucial for a wide range of industrial and technological applications. In this study, we systematically investigated the corrosion resistance of over 2105 metals, intermetallics, and metal oxides within water's stable region and identified 637 water-stable materials, including pure metals, intermetallics, and oxides. We demonstrate that the formation of intermetallic compounds or multimetallic metal oxides can further extend the aqueous stability window of a given metal species, even if the corresponding pure metal or metal oxides are inherently unstable within water. Such stabilizing effect arose from thermodynamic principles, as multimetallic, intermetallic, or metal oxide ground states need to show negative formation energy in the convex hull made from the single metal counterparts, e.g., pure metal or binary oxides. This synergy between different metals provides a valuable framework for guiding the compositional design of corrosion resistance for multimetallic systems. Our findings offer a systematic mapping and a comprehensive reference for understanding the design principles of corrosion-resistant materials.



## 1. INTRODUCTION

The aqueous stability of metal species is a critical factor for durability when metallic materials or metal oxides are employed as active materials in energy applications, such as electrocatalysis<sup>1–8</sup> and aqueous batteries.<sup>9–11</sup> Despite growing efforts to discover novel catalytic and battery materials, there remains a surprising lack of a systematic understanding of how certain materials can achieve aqueous stability. It is important to note that a material that can be synthesized and demonstrates promising performance may not always be viable for long-term material discovery, especially if it gradually dissolves in an aqueous solution. For instance, our recent high-throughput intermetallic catalysis screening identified several materials with favorable synthetic accessibility and promising overpotential as hydrogen evolution reaction (HER) or oxygen evolution reaction (OER) catalysts.<sup>5</sup> However, many of these candidates exhibit poor stability under acidic conditions, at high voltages, or in both scenarios.<sup>5</sup> This emphasizes the urgent need for rational design principles and comprehensive references to predict and control the aqueous stability of specific metal elements in various material forms, thus enabling the development of durable, high-performance materials for energy devices with extended lifetimes.

In this work, we performed a high-throughput screening based on all data available in Materials Project,<sup>12</sup> focusing on metallic and metal oxide systems encompassing 47 elements, and identified 2105 distinct water-stable compositions. Pourbaix diagrams were constructed and analyzed for all

compositions to assess the water stability window in terms of pH and redox potential (Eh). Through comprehensive data mining, we uncovered general elemental trends in the aqueous stability of metallic and oxide systems, demonstrating the potential of multimetallic systems to protect certain metal species from corrosion. Furthermore, we charted the potential of improved oxidation potential for all metals by forming intermetallics with other metal species. An interactive database<sup>13</sup> is also provided to facilitate efficient analysis and comparison of aqueous stability windows across systems.

## 2. METHODS

The stability of various inorganic materials, including pure metals, intermetallic, oxide, hydroxide, and oxyhydroxide compounds, was investigated using Pourbaix diagrams with pH ranging from 0 to 14 and voltage ranging from –2 to 2 V (vs SHE).<sup>14–16</sup> All DFT data was extracted from Materials Project with GGA/GGA+U type calculations<sup>17</sup> with necessary corrections.<sup>17–19</sup> Such treatment is usually regarded as sufficient for energetic calculations such as Pourbaix diagram analysis, as it reproduces a close enough estimation of critical energies such as mixing enthalpy. For each composition, the lowest

Received: February 24, 2025

Revised: June 12, 2025

Accepted: June 13, 2025

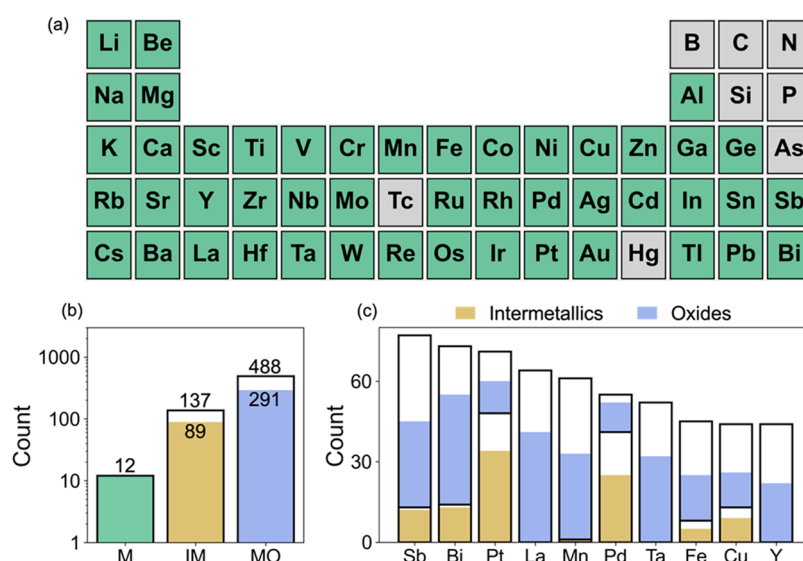


**Figure 1.** Statistics of compounds investigated in this work, all of which are water-stable compounds. (a) Periodic table with the selected elements highlighted in green and the rest in light gray. (b) Distribution of compounds across various material families: metals (M) are highlighted in green, intermetallics (IM) are highlighted in yellow, and oxides (MO) are highlighted in blue. Filled bars represent experimentally reported compounds, while open bars indicate theoretically predicted compounds that have not been experimentally reported. (c) Top 10 elements with the highest number of water-stable compounds, along with their corresponding distributions of intermetallics and oxides.

energy entry is used for constructing the Pourbaix diagram. These diagrams were generated utilizing the Python Materials Genomics (Pymatgen) package,<sup>20</sup> which accessed data from Materials Project.<sup>12</sup> The Pourbaix diagram for each compound is constructed to assess the water stability using the approach proposed by Persson et al.<sup>16</sup> Particularly, the key of the Pourbaix diagram construction process is to assume  $\Delta E_{\text{DFT}}^{\text{Solid-Aqueous}} \approx \Delta E_{\text{Experiment}}^{\text{Solid-Aqueous}}$ . All solid entries are usually estimated much more accurately in DFT calculations than aqueous species. Therefore, as long as one can obtain experimental free energy information on the aqueous species, the corresponding DFT value can be estimated with high accuracy while avoiding applying complicated computational setups. In this work, all experimental references for aqueous species are adopted from the organized data set in Materials Project.<sup>12</sup> During the analysis, all ionic concentrations are set to  $10^{-6}$  M.<sup>21</sup> This process results in a pool of 2105 compounds selected from a combination of 47 elements, which can then be categorized as 12 pure metals (which are stable in the water region), 1444 intermetallic compounds (137 compounds are stable in the water region), 578 oxide compounds (478 compounds are stable in the water region), one hydroxide compound (LaOH, which is not stable in the water region), and four oxyhydroxide compounds (CoOOH, LaOOH, AgOOH, and NiOOH, with only CoOOH and LaOOH being stable in the water region). For all of the compounds that are stable in water, we extract the vertices of the stability region for further analysis.

### 3. RESULTS

**3.1. Statistical Analysis of All Compounds.** As shown in Figure 1a, the selected metals include alkali metals, alkaline earth metals, all 3d, 4d, and 5d transition metals, and post-transition metals from groups III–V. Radioactive elements such as Tc and liquid metal Hg were excluded as they are impractical species for developing corrosion-resistant catalysts. As a result, our data mining covers 47 metal species. All Pourbaix diagrams are constructed using the methodology presented in Section 2 for statistical analysis. All entries, including both solid and aqueous species, were sourced from the Materials Project database.<sup>12</sup> The total number of compounds across three primary material types, metals, intermetallic compounds, and metal oxide compounds, are shown in Figure 1b. The number of experimentally reported

compounds is shown with filled bars, while the hypothetical compounds in the Materials Project database are shown with unfilled portions of bars. The occurrence of intermetallic and oxide compounds across the top 10 metal elements is shown in Figure 1c.

### 3.2. Aqueous Stability Trend of Pure Metals and Intermetallics.

Selected examples of pure metals and intermetallics that are water-stable are shown in Figure 2. The maximum pH window and Eh window (vs RHE) have been used for illustrating the stability trend. As shown in Figure 2a, seven noble metals, including Ru, Pd, Ag, Os, Ir, Pt, and Au, remain stable across the entire pH range from 0 to 14. Rh is the only exception, which is stable only at pH values above 2.3. The stability pH and Eh windows of non-noble metals are also demonstrated in Figure 2a,b, separated by a solid horizontal line. In contrast to noble metals, non-noble metals are generally unstable in water regions except for Co, Ni, Cu, and Bi. Among these, Cu exhibits the widest pH stability window for non-noble transition metals, spanning the pH range from 0.3 to 14.0 when the voltage is below 0.42 V (vs RHE). Co and Ni are stable within a narrower pH range of 6.7 to 8.0 and 6.4 to 14.0, respectively. As a main group metal, Bi is stable within the pH range from 8.5 to 14.0. Meanwhile, Figure 2b highlights the voltage stability window, bounded by the minimum anodic and maximum cathodic reaction voltages, for pure metals in the water region. The upper voltage limit (vs RHE) is critical for determining the oxidation resistance of pure metals and intermetallic compounds. While the general trend may appear to be intuitive, precise values for all possible anodic and cathodic reactions add quantitative insight into our analysis. As shown in Figure 2b, Au demonstrates the highest oxidation resistance, remaining stable up to 1.00 V (vs RHE), followed by Ag (0.88 V vs RHE) and Pt (0.66 V vs RHE). Among the four non-noble transition metals stable in the water region, Cu shows the highest oxidation resistance, remaining stable up to 0.42 V (vs RHE). Ni and Co are stable only at lower voltages of 0.17 and 0.03 V (vs RHE), respectively. Bi is stable in the water region at up to 0.02 V vs RHE.

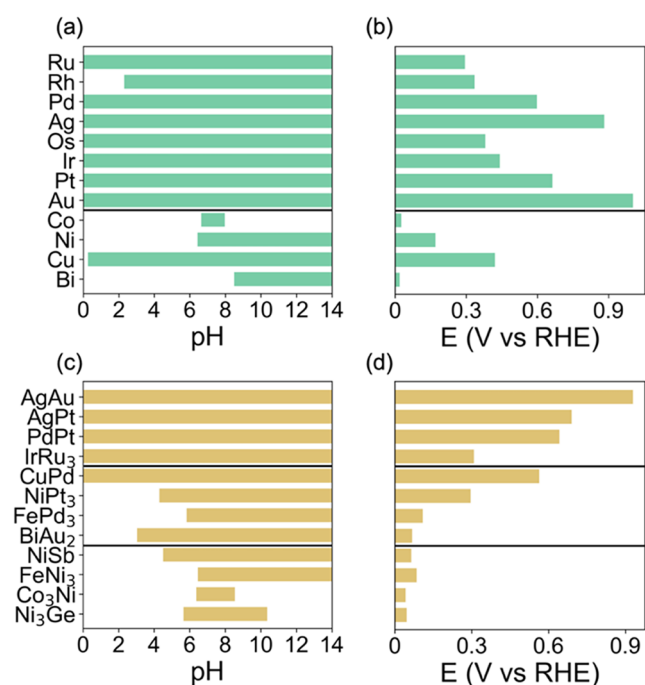


**Figure 2.** pH and voltage stability window of metals and intermetallics. (a) pH stability window of metals. The solid lines are added to distinguish the compounds by noble metal content (similar in panels (b–d)). (b) Voltage stability window of metals. The voltage is measured vs RHE. (c) pH stability window of intermetallics. The compositions of selected compounds are shown in the *y*-axis. (d) Voltage stability window of the intermetallics.

For intermetallics, we identified that 137 of 1444 intermetallic compounds are stable within the water stability window. Among these, 129 compounds contain at least one noble metal element. To further investigate the elemental dependence of aqueous stability, we categorized all 137 stable intermetallics into three groups: (a) intermetallic compounds containing only noble metals (15 compounds), (b) intermetallic compounds containing both noble and non-noble metals (114 compounds), and (c) intermetallic compounds containing only non-noble metals (8 compounds). These three groups are separated by two horizontal black lines in Figure 2c,d, with representative intermetallic compounds illustrated for each group. As shown in Figure 2c, intermetallic compounds containing only noble metals remain stable across the entire pH range (0–14) within the water stability window. In contrast, noble-metal-free intermetallics are generally stabilized in a much narrower pH range, with none exhibiting stability across the full pH spectrum. A trade-off between noble metal content and aqueous stability is found in intermetallics with a mixture of noble metals and non-noble metals, represented by CuPd, NiPt<sub>3</sub>, FePd<sub>3</sub>, BiAu<sub>2</sub>, NiSb, and Ni<sub>3</sub>Ge. Most such compounds show reasonable stability crossing both acidic and alkaline conditions. However, some compounds, such as FePd<sub>3</sub> and FeNi<sub>3</sub>, are stable primarily in alkaline conditions, while Co<sub>3</sub>Ni exhibits stability only near neutral conditions (pH ≈ 7).

In summary, for the aqueous stability of metallic materials, we found 12 pure metals and 137 intermetallics that are stable under HER conditions. However, no metallic materials remain stable under the ORR/OER voltages. Even when accounting for scaling relationships<sup>5,22–24</sup> that reduce the effective voltage (vs RHE) from 1.23 to 0.86 V or lower for ORR, only two

pure metals (Ag and Au) and three intermetallics (AgAu, AgAu<sub>3</sub>, and Ag<sub>3</sub>Au) are observed to be stable thermodynamically. It is worth noting that during ORR/OER reactions, certain pure metals or intermetallic compounds can be stabilized or passivated due to surface oxide formation<sup>25,26</sup> or kinetic stabilization when the decomposition driving force is relatively weak.<sup>5,27</sup> These factors could further expand the range of viable metallic materials for the OER/ORR reactions.

### 3.3. Binary and Multinary Metal Oxide Compounds.

Metal oxide compounds are typical solid products formed when metal species undergo oxidation in water. Metals can produce various types of oxides across different pH levels and voltages by varying their oxidation states. For instance, Mn can form Mn<sub>3</sub>O<sub>4</sub>, Mn<sub>2</sub>O<sub>3</sub>, and MnO<sub>2</sub> at various pH values and voltages (see Figure S1). When considering multicomponent systems, the resulting Pourbaix diagrams become more complex. In this section, we first map the pH and voltage stability windows for all binary oxides. Subsequently, we demonstrate the potential mechanisms for multinary oxides to be stabilized in water.

Figure 3 summarizes the stability windows for pH (Figure 3a) and Eh (Figure 3b) for binary metal oxides. Fifteen metal species, Li, Na, K, Rb, Cs, Mg, Ca, Sr, Ba, Nb, Co, Cd, La, Re, and Au, do not have oxides stable in water and thus are not shown in the figure. Different opacities represent various oxidation states, with higher opacities corresponding to elevated oxidation numbers. The oxidation states of metal oxides are determined based on their chemical formulas and confirmed by literature reports. For example, the metals in RuO<sub>4</sub> and OsO<sub>4</sub> are assigned an oxidation state of +8, as supported by the literature.<sup>28–31</sup> Metals are arranged according to their positions in the periodic table, with the exception of Be and Al, which are placed at the very end of the sixth row elements for better balanced alignment across three panels. It can be indicated by Figure 3 that oxide compounds are generally more stable under alkaline conditions. Additionally, many non-noble metal oxides remain stable in highly acidic environments (pH < 3), as summarized in Table 1. Most noble metal oxides are also stable under acidic conditions, except for AgO, which is only stable at pH > 8.0. Meanwhile, the majority of the water-stable metal oxides (29 out of 49) remain stable at pH = 14, with exceptions summarized in Table 2.

Clear and well-defined trends are observed in Figure 3b when comparing the voltage window and the pH window. The stable oxidation states of specific metals generally follow an ascending order with increasing voltage. Meanwhile, the voltage ranges of different metal oxidation states often tend to complement each other. The voltage stability range also compensates for the oxidation limits of water-stable metals, e.g., noble metals and Co, Ni, and Cu, as evidenced by Figures 2 and 3. Overall, it can be concluded that many metal solids that exhibit water-stable regions, whether in elemental or oxide form, remain stable across the entire voltage span of water (0–1.23 V vs RHE), with the exception of metals such as Co, Tl, Sb, and Au and their oxides. The metal species that do not have solid phases (pure metal or metal oxides) spanning the electrochemical water stability range (0–1.23 V vs RHE) are listed in Table 3, with the lower and upper bounds indicating their voltage stability window. The voltage (E) is referenced to RHE.

With the stability trend established in binary oxides, we further extend our analysis to multinary oxides. To develop an understanding of potential synergistic effects in a multimetallic

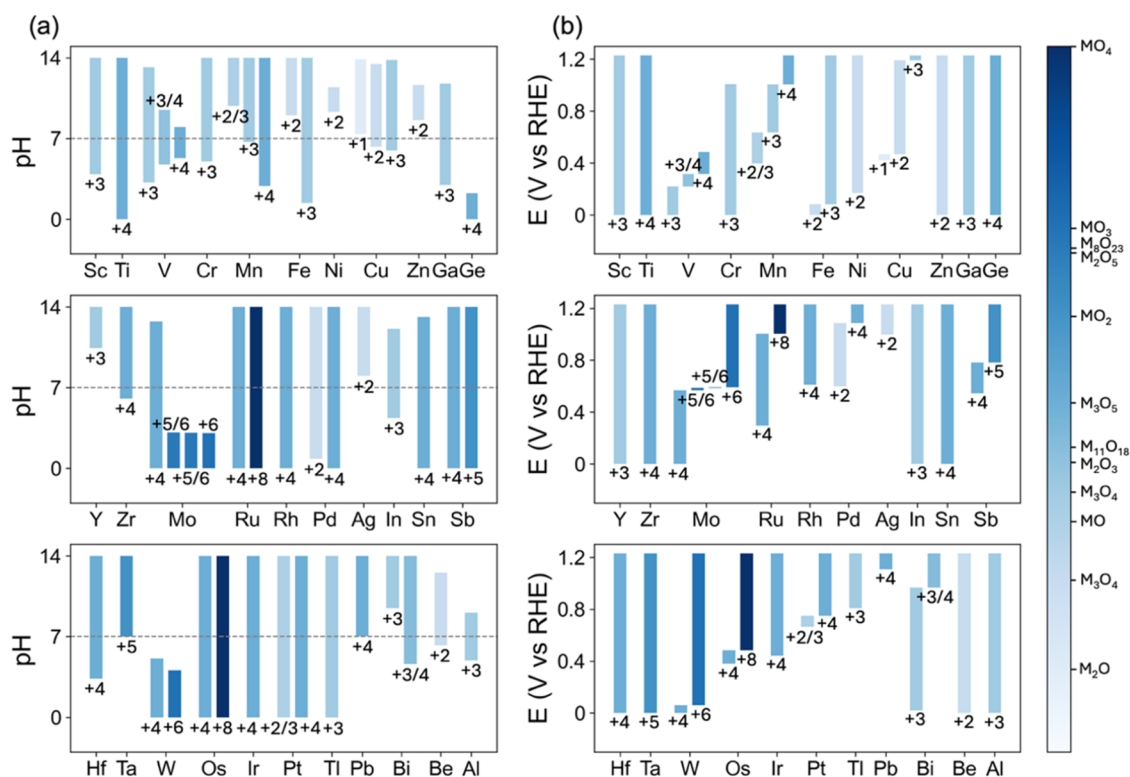


**Figure 3.** pH and Eh windows of the binary oxides. For both subfigures, the elements in the same row are organized in the same panel, except that Be and Al are organized with sixth row elements for a balanced view. Corresponding oxidation numbers of metals are indicated by both color and notations. (a) pH stability window. The gray dashed line represents pH = 7. (b) Anodic stability window of binary oxides is denoted as E (V vs RHE, where RHE is the reversible hydrogen electrode). The style is similar to (a). The corresponding chemical formulas of binary oxides are indicated as labels in the color bar shown on the right. Note that for Mo, the two bars containing both +5 and +6 oxidation states are approximations of oxidation number in  $\text{Mo}_8\text{O}_{23}$  and  $\text{Mo}_9\text{O}_{26}$ .

**Table 1.** pH Stability Window of Water-Stable Binary Oxides Which Are Stable at pH < 3<sup>a</sup>

composition	pH range	composition	pH range	composition	pH range
TiO <sub>2</sub>	[0.0, 14.0]	IrO <sub>2</sub>	[0.0, 14.0]	Mo <sub>9</sub> O <sub>26</sub>	[0.0, 3.1]
RuO <sub>2</sub>	[0.0, 14.0]	PtO <sub>2</sub>	[0.0, 14.0]	MoO <sub>3</sub>	[0.0, 3.1]
RuO <sub>4</sub>	[0.0, 14.0]	Pt <sub>3</sub> O <sub>4</sub>	[0.0, 14.0]	GeO <sub>2</sub>	[0.0, 2.3]
RhO <sub>2</sub>	[0.0, 14.0]	Tl <sub>2</sub> O <sub>3</sub>	[0.0, 14.0]	PdO	[0.8, 14.0]
PdO <sub>2</sub>	[0.0, 14.0]	SnO <sub>2</sub>	[0.0, 13.1]	Fe <sub>2</sub> O <sub>3</sub>	[1.4, 14.0]
SbO <sub>2</sub>	[0.0, 14.0]	MoO <sub>2</sub>	[0.0, 12.7]	MnO <sub>2</sub>	[2.9, 14.0]
Sb <sub>2</sub> O <sub>5</sub>	[0.0, 14.0]	WO <sub>2</sub>	[0.0, 5.1]	V <sub>2</sub> O <sub>3</sub>	[2.9, 13.1]
OsO <sub>2</sub>	[0.0, 14.0]	WO <sub>3</sub>	[0.0, 4.1]	Ga <sub>2</sub> O <sub>3</sub>	[3.0, 11.8]
OsO <sub>4</sub>	[0.0, 14.0]	Mo <sub>8</sub> O <sub>23</sub>	[0.0, 3.2]		

<sup>a</sup>The compounds are sorted according to the lower bound of pH stability window from low to high.

system, the stability of multinary oxides is in contrast with binary oxides with the same oxidation numbers. Taking an arbitrary ternary oxide,  $\text{A}_x\text{B}_y\text{O}_z$ , as an example, we will visualize their stability windows with two corresponding binary oxides ( $\text{AO}_x$  and  $\text{BO}_y$ ) with the same oxidation states to directly show whether there is an extension of the stability window. To apply

**Table 2.** pH Stability Window of Water-Stable Metal Oxides Which Are Unstable at pH = 14<sup>a</sup>

composition	pH range	composition	pH range	composition	pH range
GeO <sub>2</sub>	[0.0, 2.3]	Al <sub>2</sub> O <sub>3</sub>	[4.9, 9.1]	MoO <sub>2</sub>	[0.0, 12.7]
MoO <sub>3</sub>	[0.0, 3.1]	V <sub>5</sub> O <sub>5</sub>	[4.7, 9.5]	V <sub>2</sub> O <sub>3</sub>	[2.9, 13.1]
Mo <sub>9</sub> O <sub>26</sub>	[0.0, 3.1]	NiO	[9.3, 11.4]	SnO <sub>2</sub>	[0.0, 13.1]
Mo <sub>8</sub> O <sub>23</sub>	[0.0, 3.2]	ZnO	[8.6, 11.6]	CuO	[6.3, 13.5]
WO <sub>3</sub>	[0.0, 4.1]	Ga <sub>2</sub> O <sub>3</sub>	[3.0, 11.8]	Cu <sub>2</sub> O <sub>3</sub>	[6.0, 13.8]
WO <sub>2</sub>	[0.0, 5.1]	In <sub>2</sub> O <sub>3</sub>	[4.4, 12.1]	Cu <sub>2</sub> O	[7.4, 13.9]
VO <sub>2</sub>	[5.3, 8.0]	BeO	[6.2, 12.5]		

<sup>a</sup>The compounds are sorted according to the upper bound of the pH stability window from low to high.

such analysis to 346 water-stable ternary oxides, all materials can be classified into three main groups (as shown in Figure 4): (1) the first group (denoted as group I) includes 81 ternary oxides, where both corresponding binary oxides are stable and share overlapping stability windows; (2) the second group (denoted as group II) consists of 26 ternary oxides, where both corresponding binary oxides are stable in water, but their stability windows do not overlap within the water stability region; (3) the third group (denoted as group III) encompasses 239 ternary oxides, where at least one binary

**Table 3. Voltage Stability Window of Metal Solids (Elements and Binary Metal Oxides) Which Does Not Span the Full Voltage Range<sup>a</sup>**

metal	voltage range (V vs RHE)	metal	voltage range (V vs RHE)
Co	[0.00, 0.03]	Sb	[0.54, 1.23]
Pb	[1.11, 1.23]	Mn	[0.40, 1.23]
Tl	[0.81, 1.23]	Au	[0.00, 1.00]
V	[0.00, 0.48]	Cr	[0.00, 1.00]

<sup>a</sup>The metal solids are sorted according to the voltage stability window range from low to high. All voltages are referenced to RHE.

oxide counterpart (or both) is not stable in water stability region.

One ternary oxide is selected from each category to illustrate the general stability trend in Figure 4. Figure 4a–c illustrates the aqueous stability window for multinary oxides in the first group, using FeSbO<sub>4</sub> as an example. With reference binary counterparts being Fe<sub>2</sub>O<sub>3</sub> and Sb<sub>2</sub>O<sub>5</sub>, shown in Figure 4a, the stability windows of Fe<sub>2</sub>O<sub>3</sub> and Sb<sub>2</sub>O<sub>5</sub> largely overlap, as further evidenced by the one-dimensional plots in Figure 4b,c. Consequently, the stability window of FeSbO<sub>4</sub> includes all of the overlapping regions of the binary oxides and extends slightly beyond these regions. The extended stability can be

attributed to the negative reaction energy for the formation reaction  $\text{Fe}_2\text{O}_3 + \text{Sb}_2\text{O}_5 \rightarrow \text{FeSbO}_4$ , as FeSbO<sub>4</sub> is the ground state on the pseudobinary hull of Fe<sub>2</sub>O<sub>3</sub>–Sb<sub>2</sub>O<sub>5</sub>. Since FeSbO<sub>4</sub> exhibits lower energy than the solid forms of Fe<sup>3+</sup> and Sb<sup>5+</sup> compared to binary oxides, its stability window expands beyond the overlapping region of the binary oxides. In general, when both binary oxides are stable and possess overlapping stability windows, the corresponding ternary oxide is also stable within this overlapped area. Additionally, the negative formation energy from the binary oxides will further expand its stability window beyond the overlapped area. In contrast, Figure 4d–f demonstrates that the energy lowering in certain ternary oxides can be sufficient to stabilize them without requiring overlapping stability windows of their binary counterparts. Y<sub>3</sub>Al<sub>5</sub>O<sub>12</sub> is an example where the corresponding binary oxides, Y<sub>2</sub>O<sub>3</sub> and Al<sub>2</sub>O<sub>3</sub>, do not share overlapping stability windows. Specifically, Y<sub>2</sub>O<sub>3</sub> will transfer into the Y<sup>3+</sup> ion in the stable region of Al<sub>2</sub>O<sub>3</sub>, while Al<sub>2</sub>O<sub>3</sub> forms Al(OH)<sub>4</sub><sup>−</sup> or Al<sub>11</sub>O<sub>18</sub> at the stability window of Y<sub>2</sub>O<sub>3</sub>. However, in the case of Y<sub>3</sub>Al<sub>5</sub>O<sub>12</sub>, the formation energy of −1.335 eV/atom from Y<sub>2</sub>O<sub>3</sub> and Al<sub>2</sub>O<sub>3</sub> makes it stable against Y<sup>3+</sup> and Al(OH)<sub>4</sub><sup>−</sup>/Al<sub>11</sub>O<sub>18</sub> over a wide range of pH and voltage, as shown in Figure 4e,f. Finally, Figure 4g–i demonstrates that if the formation of a ternary oxide from binary oxides results in

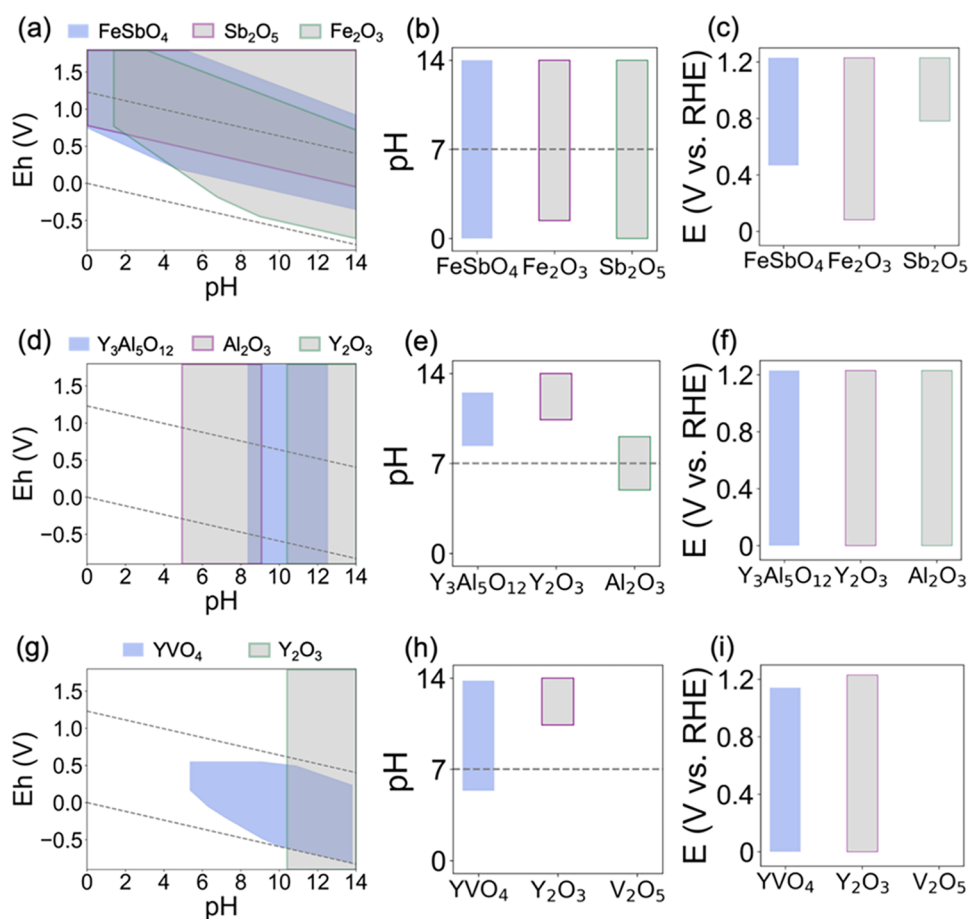


**Figure 4.** Stability window of ternary oxides. (a), (d), and (g) Examples of three categories of stabilization modes, e.g., FeSbO<sub>4</sub>, Y<sub>3</sub>Al<sub>5</sub>O<sub>12</sub>, and YVO<sub>4</sub>, respectively. The blue color indicates the stable region of the ternary oxide. The gray polygons with green and purple borders indicate the stability regions of decomposed binary oxides, respectively. The gray dashed lines represent the HER (lower) and ORR (upper) lines, respectively. (b), (e), and (h) pH stability windows of corresponding ternary oxides and their reference binary oxides with the same oxidation number, following the same color scheme as (a), (d), and (g). (c), (f), and (i) Voltage stability windows of ternary oxide compounds (FeSbO<sub>4</sub>, Y<sub>3</sub>Al<sub>5</sub>O<sub>12</sub>, and YVO<sub>4</sub>, respectively) and their reference binary oxides with the same oxidation number, following the same color scheme.

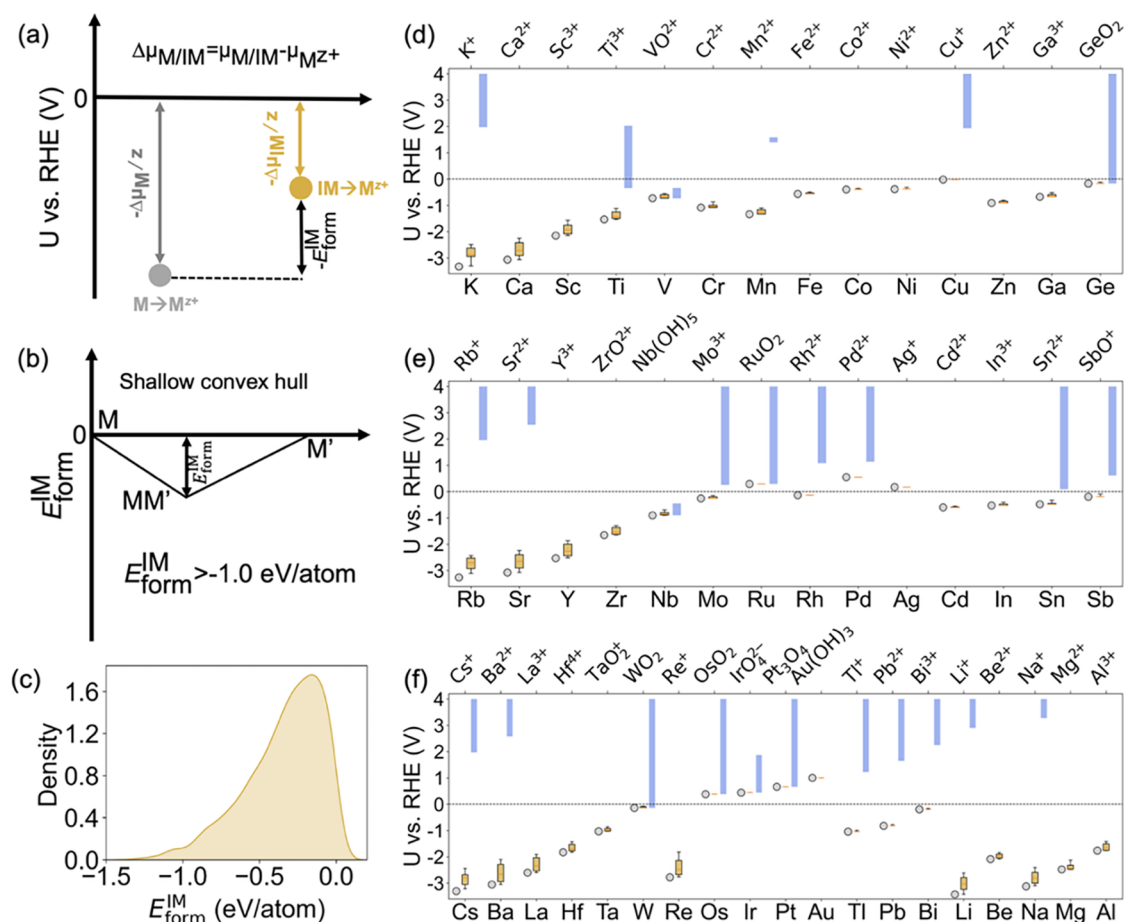


**Figure 5.** (a) Schematic of the elevation of metal oxidation potential by forming intermetallic; (b) schematic of the convex hull for intermetallic formation energies; (c) probability distribution of intermetallic formation energies; and (d–f) comparison of standard oxidation potentials of pure metal (silver dot) and metal in corresponding intermetallics (yellow boxplot) and voltage windows of corresponding metal oxides. Elements Li, Be, Na, Mg, and Al from the second and third rows are shown at the end of panel (f). The blue bars represent the stability window of metal oxides under the given conditions, with only the targeted metal present in the aqueous solution.

sufficiently negative formation energy, the corresponding binary oxides do not need to be stable in the water.  $YVO_4$  is an example of this case, as shown in Figure 4g, where only one of the decomposing binary oxides,  $Y_2O_3$ , is stable in the water region, while the other counterpart,  $V_2O_5$ , is not. We found that this general trend also holds for multinary oxides containing more than two metals. Specifically, 91 out of the multinary oxides with  $n_{metal} > 2$  are stable in water, with 20 compounds falling into the scenario of group I, 10 compounds under group II, and 61 under group III.

## 4. DISCUSSION

**4.1. Chemical Principles for Aqueous Stability.** One concept becomes increasingly clearer from the analysis presented in Figures 2–4: the corrosion resistance of a potential compound is determined by the competition between the stabilization of a limited amount of ions and the extent of bonding strengths when forming solid phases. When the solid phase becomes multicomponent, there could be further spaces to expand the aqueous stability. Enhanced bonding strength can be directly quantified by the negativity of the formation energy. In this section, we will rationalize how formation energy influences the aqueous stability. Particularly, we will focus on multinary intermetallics, trying to establish an extendable voltage window in acidic environment (pH = 0).

In general, intermetallics and metals in acidic environments will be stable at low enough voltage, while the major competing reaction is either the dissolution as aqueous species or the formation of metal oxides. Mechanistic schematics of how the formation of intermetallics can broaden the voltage window of a specific metal are demonstrated in Figure 5a. From a thermodynamic perspective, the oxidation potential from an elemental metal to its most stable aqueous species,  $M^{z+}$ , can be determined from the condition where the chemical potential of the metal in its elemental state is balanced by the chemical potential of its ionic species and the electrons in solution, as expressed in the following equation

$$\mu_M = \mu_{M^{z+}} + z\mu_{e^-} = \mu_{M^{z+}} - zU \quad (1)$$

where  $z$  is the positive charge of the metal carriers,  $\mu_{e^-}$ , defined by the chemical potential of the electron, can be quantified as  $-U$  per electron. With this consideration, the oxidation potential  $U_{oxi}^M$  will be calculated as

$$U_{oxi}^M = (\mu_M - \mu_{M^{z+}})/-z = -\Delta\mu_M/z \quad (2)$$

Similarly, the oxidation potential of intermetallic  $U_{oxi}^{IM}$  can be expressed as

$$U_{oxi}^{IM} = (\mu_{IM} - \mu_{M^{z+}})/-z = -\Delta\mu_{IM}/z \quad (3)$$

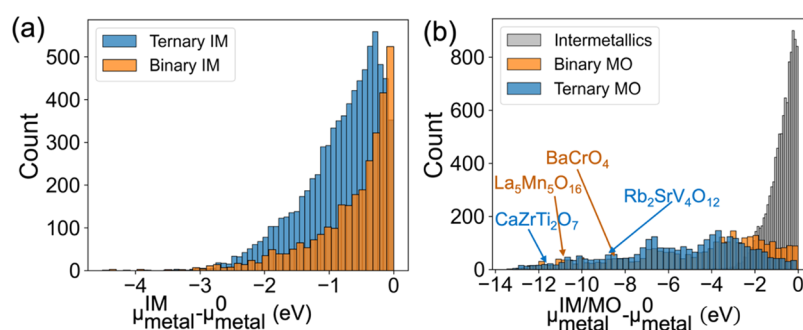


**Figure 6.** (a) Chemical potential of metal in binary intermetallics and ternary intermetallics. The most stable elemental metal phase is used as a reference. (b) Chemical potential of metals in binary/ternary metal oxides, in contrast to binary/ternary intermetallics.

As indicated by eqs 2 and 3, when the intermetallic compound has a negative formation energy, this means that the compound is more stable than its elemental phases. Since chemical potential is the first derivative of free energy, this stability implies that the chemical potential of metal in intermetallic is lower than or equal to that in the pure metal phase. Because the oxidation potential  $U_{\text{oxi}}$  is influenced by the chemical potential of the metal, a lower  $\mu_{\text{IM}}$  results in a higher or equal  $U_{\text{oxi}}^{\text{IM}}$  compared to that of  $U_{\text{oxi}}^{\text{M}}$ . Therefore,  $U_{\text{oxi}}^{\text{IM}}$  will always be equal to or greater than  $U_{\text{oxi}}^{\text{M}}$  when the intermetallic material has a negative formation energy. In other words, intermetallic compounds that lie on the convex hull are inherently more or equally corrosion-resistant than elemental metals. Consequently, the metal in the intermetallic phase will oxidize at higher potentials compared to its elemental form. The maximum increase in the oxidation potential is essentially  $-E_{\text{form}}^{\text{IM}}$ . In some cases, the aqueous competing phases will include O and H, which will make the actual elevation of oxidation potential of targeted metal species lower than  $-E_{\text{form}}^{\text{IM}}$ , as part of the formation energies are contributed to lower down the energy of O and H rather than the metal. However, it will not change the trend that forming intermetallic will strengthen the corrosion resistance of specific metals in general. In summary, the use of intermetallic compounds can effectively protect certain metal species from oxidation and dissolution.<sup>21</sup>

It is important to note that the protective effect of an intermetallic compound is quite limited, as the formation energy of typical intermetallics is generally not smaller than  $-1.0$  eV/atom. This characteristic is illustrated in Figure 5b, while the actual distribution of all intermetallics is shown in Figure 5c. Consequently, if a metal is prone to oxidation and dissolution in an aqueous solution at U vs RHE values significantly lower than  $-1.0$  V, it is unlikely that the formation of intermetallic compounds will be sufficient to stabilize the metal against water. The elemental dependence of the oxidation potential for all considered metals is presented in Figure 5d–f. A complete version of the stability window of all phases with a given metal can be found in Figure S2. It can be seen that the oxidation potential of a metal in an intermetallic compound is generally equal to or higher than that of the metal in its elemental state. This indicates that intermetallic formation provides some degree of stabilization against oxidation and dissolution. In Figure 5d, highly reactive metals such as K, Ca, and Sc exhibit strongly negative oxidation potentials, making them susceptible to oxidation and dissolution in aqueous environments. Moving toward the right, metals like Fe, Co, Ni, Cu, and Zn show oxidation

potentials closer to 0 V vs RHE, indicating that these metals have better stability against oxidation. The effect of intermetallic formation is more pronounced for highly reactive metals, as seen from the larger spread in oxidation potentials for those elements in intermetallics compared to transition metals and noble metals. Figure 5e,f shows similar trends for metals from rows 5 and 6 of the periodic table. Elements such as Rb, Sr, Y, and Zr in Figure 5e and Cs, Ba, La, Hf, and Re in Figure 5f also exhibit low oxidation potentials, revealing a strong tendency for oxidation and dissolution. Meanwhile, noble metals such as Ir, Pt, and Au have much higher oxidation potentials, making them highly stable against oxidation. Although intermetallic formation raises the oxidation potential, its effect is limited, particularly for metals that already have oxidation potentials close to or above 0 V vs RHE. This suggests that while intermetallics can improve oxidation resistance, they are insufficient to fully protect highly reactive metals from dissolution in aqueous environments.

To provide more quantitative insight into the potential for enhancing the corrosion resistance of specific metals, we constructed a histogram of all ground-state binary and ternary intermetallics and metal oxides from the Materials Project database, categorized by their chemical potentials relative to the corresponding pure metal ground states. For intermetallic compounds, the reduction in chemical potential essentially indicates the extent to which the oxidation potential of the corresponding metal can be increased. As shown in Figure 6a, most binary intermetallics achieve a chemical potential reduction of less than  $-2$  eV/atom. Ternary intermetallics perform slightly better, extending the reduction range to approximately  $-3$  eV/atom. However, as illustrated in Figure 6b, the stabilization significantly lowers the chemical potential of the corresponding metal, reaching values as low as  $-12$  eV/atom or even lower. The materials exhibiting the 100 lowest values are listed in Table S1. This pronounced reduction in  $\mu_{\text{metal}}$  is particularly evident in oxygen-rich compounds, with examples highlighted in Figure 6b. It is important to note that the relationship between negative  $\mu_{\text{metal}}$  and the electrochemical stability window is complex for oxides as equilibrium must be achieved with electrons and oxygen under specific aqueous conditions (e.g., at a given voltage and pH). Nevertheless, the substantially more negative  $\mu_{\text{metal}}$  values and the broader distribution observed for multimetallic oxides indicate a much greater tunable space for optimizing the corrosion resistance.

**4.2. Synergistic Effects for Metal Interaction.** Aside from the rationale of the stabilization mechanism for intermetallics, another important perspective is how the

formation of multimetallic systems will enhance the corrosion resistance of certain metal species. More specifically, a quantitative understanding of the elemental dependent synergistic effect in terms of the broadening voltage window will be useful. By analyzing all 1624 binary intermetallics that are ground states in the phase diagram, a heatmap that shows the frequency when a certain metal has an expanded stability window has been shown in Figure 7. All targeted metals are

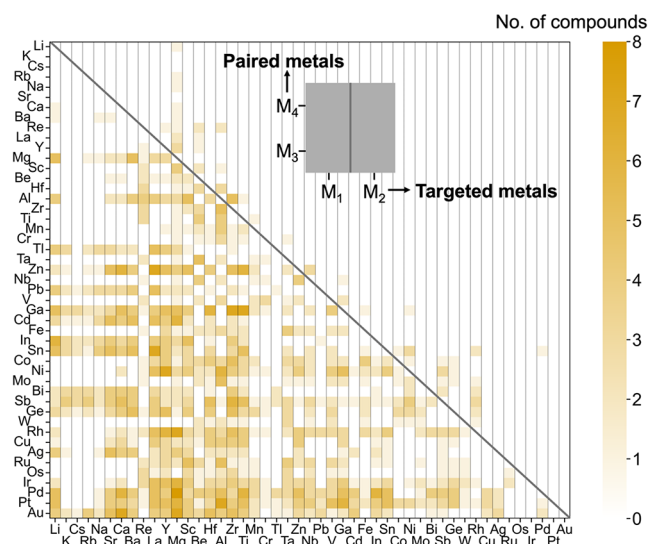


**Figure 7.** Heatmap of the synergistic effect observed in binary intermetallics. The metals on the  $x$ -axis are arranged according to their redox potential in their elemental state, while the  $y$ -axis follows the same ordering. Each cell quantifies the number of intermetallics in which the metal element on the  $x$ -axis exhibits a higher oxidation potential when forming an intermetallic with the element on the  $y$ -axis. The diagonal gray line represents the boundary where all cells below it correspond to combinations in which the targeted metal has a lower oxidation potential than the paired metal. The intensity of the yellow color represents the number of intermetallic compositions, with a higher opacity (darker shades) indicating a greater number of compounds exhibiting synergistic effects.

displayed as the  $x$ -axis of the heatmap, following the order of their redox potential at the elemental phase. The color block intersecting with each row indicates the amount of intermetallic that will improve the oxidation potential of the targeted metal. The corresponding color bars are shown on the right side of the heatmap. Additionally, Table S2 provides a comprehensive list of metal pairs demonstrating potential synergistic effects.

From the right to left of the figure, the  $x$ -axis follows the ascending order of oxidation potential, as calculated in Figure 5. It can be guided by the diagonal gray line that almost all synergistic metal pairs occur when the targeted metal has a lower oxidation potential than the paired metal. That means the negative formation energy brought by metal interactions in intermetallics is more effective when the paired metal has a higher oxidation limit than the targeted metal. When the paired metal has a lower oxidation limit than the target metal, the dropping of the chemical potential of the targeted metal by forming intermetallic should be negative enough to compensate for the redox potential differences between the two metals. Otherwise, the paired metal will simply dissolve when the redox potential is not even as high as the oxidation potential of the targeted metal. Nevertheless, there are indeed exceptions,

as shown in Figure 7. For instance,  $\text{SnPd}_3$  can push up the oxidation potential of Pd from 0.55 to 0.77 V, even if Sn metal will be oxidized at  $-0.48$  V. This is mainly due to the formation energy of  $\text{SnPd}_3$  being as low as  $-2.08$  eV per Sn site, which is sufficient to compensate the oxidation potential differences between Pd and Sn. Moreover, there are overall 67 cases when the targeted metal can have higher oxidation potential even by forming an intermetallic with a metal that shows lower oxidation potential, represented by Be–Y, Ti–Mn, and Fe–Ga–based intermetallics. Such observations also offer opportunities to further enhance the stability of noble metals (Rh and Pd), given that their oxidation potentials are usually higher than most other metals (also shown in Figures 2 and 5), making it challenging for further stabilization according to the rules we found. Moreover, several non-noble metals that are fairly unstable in an aqueous environment, such as Be, Mg, Al, Zr, Ti, Mn, Fe, Co, Ni, Ga, Ge, Y, Nb, Sb, and Ta, can have the potential to be stabilized in water by careful compositional design. It is also worth noting that the general trends discussed should not be limited to intermetallics and metal oxides. These trends are expected to apply broadly to all metal-containing crystalline solids, although additional Pourbaix diagrams may be needed for quantitative analysis.

## 5. CONCLUSIONS

This work systematically studies the stability of metals, intermetallic compounds, and metal oxides in an aqueous environment at typical corrosion conditions, for example, the metal ion concentration being  $10^{-6}$  M. Moreover, the origin of extended aqueous stability by forming multinary compounds is explained as the strengthening of chemical bonds in solids by forming higher dimensional ground states. A synergistic map has been developed to illustrate the synergistic effects of enhanced aqueous stability windows by forming intermetallics. This work can serve as a comprehensive reference for the rationale of the design of aqueous stable intermetallics and metal oxides.

## ■ ASSOCIATED CONTENT

### Data Availability Statement

The data supporting the findings are available within the main text and the SI. The data set and the interactive web application developed in this work are available at <https://jeff-oakley.github.io/M3AqueousStabilityDataSet/Index.html>.

### Supporting Information

The Supporting Information is available free of charge at <https://pubs.acs.org/doi/10.1021/acs.chemmater.5c00455>.

Example of Pourbaix diagram; stability windows of all solid phases with given metals; top 100 lowest elemental chemical potentials in multinary metal oxides, enhancing stability in water; and a complete list of synergistic effects of intermetallics (PDF)

## ■ AUTHOR INFORMATION

### Corresponding Authors

**Bin Ouyang** – Department of Chemistry and Biochemistry, Florida State University, Tallahassee, Florida 32304, United States; [orcid.org/0000-0002-8181-6815](https://orcid.org/0000-0002-8181-6815); Email: [bouyang@fsu.edu](mailto:bouyang@fsu.edu)

**Yan Zeng** – Department of Chemistry and Biochemistry, Florida State University, Tallahassee, Florida 32304, United States; Email: [zeng@chem.fsu.edu](mailto:zeng@chem.fsu.edu)

## Authors

**Yizhan Zhang** – Department of Chemistry and Biochemistry, Florida State University, Tallahassee, Florida 32304, United States

**Lin Wang** – Department of Chemistry and Biochemistry, Florida State University, Tallahassee, Florida 32304, United States

**Elena Scivally** – Department of Chemistry and Biochemistry, Florida State University, Tallahassee, Florida 32304, United States; [orcid.org/0009-0008-8138-550X](https://orcid.org/0009-0008-8138-550X)

**Kayla James** – Department of Chemistry and Biochemistry, Florida State University, Tallahassee, Florida 32304, United States; [orcid.org/0009-0005-0187-4732](https://orcid.org/0009-0005-0187-4732)

**Evelyn McBride** – Department of Chemistry and Biochemistry, Florida State University, Tallahassee, Florida 32304, United States

**Mahesh Dheerasinghe** – Department of Chemistry and Biochemistry, Florida State University, Tallahassee, Florida 32304, United States; [orcid.org/0009-0004-2078-8779](https://orcid.org/0009-0004-2078-8779)

**Michael Shatruk** – Department of Chemistry and Biochemistry, Florida State University, Tallahassee, Florida 32304, United States

Complete contact information is available at:

<https://pubs.acs.org/10.1021/acs.chemmater.5c00455>

## Author Contributions

<sup>†</sup>Y.Zhang and L.W. contributed equally to this work. Y.Zhang, Y.Zeng, and B.O. conceived the research and designed the study. Y.Zhang, L.W., Y.Zeng, and B.O. performed the data mining and computational analysis. B.O. conducted the theoretical analysis of the data, supervised the project, provided critical feedback, and helped guide the research. All authors discussed the results, contributed to the final manuscript, and gave final approval for publication.

## Notes

The authors declare no competing financial interest.

## ACKNOWLEDGMENTS

The authors would like to acknowledge the startup fund from Florida State University, as well as the support from ACS-PRF. The Computational resources are provided by the Advanced Cyberinfrastructure Coordination Ecosystem: Services & Support (ACCESS), the National Energy Research Scientific Computing Center (NERSC), a DOE Office of Science User Facility supported by the Office of Science and the U.S. Department of Energy under contract No. DE-AC02-05CH11231 and Research Computing Center (RCC) at Florida State University. The computation and data processing are also supported by the supercomputing resources from the Department of Energy's Office of Energy Efficiency and Renewable Energy at the National Renewable Energy Laboratory (NREL). The authors also want to thank Dr. Zhengda He for helpful input to this work.

## REFERENCES

- (1) Bueno, S. L. A.; Ashberry, H. M.; Shafei, I.; Skrabalak, S. E. Building Durable Multimetallic Electrocatalysts from Intermetallic Seeds. *Acc. Chem. Res.* **2021**, *54* (7), 1662–1672.
- (2) Kar, N.; McCoy, M.; Wolfe, J.; Bueno, S. L. A.; Shafei, I. H.; Skrabalak, S. E. Retrosynthetic design of core–shell nanoparticles for thermal conversion to monodisperse high-entropy alloy nanoparticles. *Nat. Synth.* **2024**, *3* (2), 175–184.

- (3) Bower, M. M.; DeSantis, C. J.; Skrabalak, S. E. A Quantitative Analysis of Anions and pH on the Growth of Bimetallic Nanostructures. *J. Phys. Chem. C* **2014**, *118* (32), 18762–18770.
- (4) Roduner, E. Selected fundamentals of catalysis and electrocatalysis in energy conversion reactions—A tutorial. *Catal. Today* **2018**, *309*, 263–268.
- (5) He, Z. D.; Ouyang, B. Charting the electronic structure for discovering low-cost intermetallic catalysts. *J. Mater. Chem. A* **2024**, *12* (33), 21987–21996.
- (6) Clarke, T. B.; Krushinski, L. E.; Vannoy, K. J.; Colon-Quintana, G.; Roy, K.; Rana, A.; Renault, C.; Hill, M. L.; Dick, J. E. Single Entity Electrocatalysis. *Chem. Rev.* **2024**, *124* (15), 9015–9080.
- (7) Seh, Z. W.; Kibsgaard, J.; Dickens, C. F.; Chorkendorff, I.; Nørskov, J. K.; Jaramillo, T. F. Combining theory and experiment in electrocatalysis: Insights into materials design. *Science* **2017**, *355* (6321), No. eaad4998.
- (8) Nørskov, J. K.; Rossmeisl, J.; Logadottir, A.; Lindqvist, L.; Kitchin, J. R.; Bligaard, T.; Jonsson, H. Origin of the Overpotential for Oxygen Reduction at a Fuel-Cell Cathode. *J. Phys. Chem. B* **2004**, *108* (46), 17886–17892.
- (9) Liang, Y.; Yao, Y. Designing modern aqueous batteries. *Nat. Rev. Mater.* **2023**, *8* (2), 109–122.
- (10) Ahn, H.; Kim, D.; Lee, M.; Nam, K. W. Challenges and possibilities for aqueous battery systems. *Commun. Mater.* **2023**, *4* (1), No. 37.
- (11) Chao, D.; Zhou, W.; Xie, F.; Ye, C.; Li, H.; Jaroniec, M.; Qiao, S. Z. Roadmap for advanced aqueous batteries: From design of materials to applications. *Sci. Adv.* **2020**, *6* (21), No. eaba4098.
- (12) Jain, A.; Ong, S. P.; Hautier, G.; Chen, W.; Richards, W. D.; Dacek, S.; Cholia, S.; Gunter, D.; Skinner, D.; Ceder, G.; et al. Commentary: The Materials Project: A materials genome approach to accelerating materials innovation. *APL Mater.* **2013**, *1* (1), No. 011002, DOI: [10.1063/1.4812323](https://doi.org/10.1063/1.4812323).
- (13) Ouyang, B. Aqueous Stability of Metals, Intermetallics and Metal Oxides, <https://jeff-oakley.github.io/M3AqueousStabilityDataSet/Index.html> (accessed Feb 24, 2025).
- (14) Singh, A. K.; Zhou, L.; Shinde, A.; Suram, S. K.; Montoya, J. H.; Winston, D.; Gregoire, J. M.; Persson, K. A. Electrochemical Stability of Metastable Materials. *Chem. Mater.* **2017**, *29* (23), 10159–10167.
- (15) Patel, A. M.; Nørskov, J. K.; Persson, K. A.; Montoya, J. H. Efficient Pourbaix diagrams of many-element compounds. *Phys. Chem. Chem. Phys.* **2019**, *21* (45), 25323–25327.
- (16) Persson, K. A.; Waldwick, B.; Lazic, P.; Ceder, G. Prediction of solid–aqueous equilibria: Scheme to combine first-principles calculations of solids with experimental aqueous states. *Phys. Rev. B* **2012**, *85* (23), No. 235438.
- (17) Jain, A.; Hautier, G.; Ong, S. P.; Moore, C. J.; Fischer, C. C.; Persson, K. A.; Ceder, G. Formation enthalpies by mixing GGA and GGA+U calculations. *Phys. Rev. B* **2011**, *84* (4), No. 045115.
- (18) Wang, A.; Kingsbury, R.; McDermott, M.; Horton, M.; Jain, A.; Ong, S. P.; Dwaraknath, S.; Persson, K. A. A framework for quantifying uncertainty in DFT energy corrections. *Sci. Rep.* **2021**, *11* (1), No. 15496.
- (19) Wang, L.; Maxisch, T.; Ceder, G. Oxidation energies of transition metal oxides within the GGA+U framework. *Phys. Rev. B* **2006**, *73* (19), No. 195107.
- (20) Ong, S. P.; Richards, W. D.; Jain, A.; Hautier, G.; Kocher, M.; Cholia, S.; Gunter, D.; Chevrier, V. L.; Persson, K. A.; Ceder, G. Python Materials Genomics (pymatgen): A robust, open-source python library for materials analysis. *Comput. Mater. Sci.* **2013**, *68*, 314–319.
- (21) McCafferty, E. *Introduction to Corrosion Science*; Springer Science & Business Media, 2010.
- (22) Zhao, Z. J.; Liu, S. H.; Zha, S. J.; Cheng, D. F.; Studt, F.; Henkelman, G.; Gong, J. L. Theory-guided design of catalytic materials using scaling relationships and reactivity descriptors. *Nat. Rev. Mater.* **2019**, *4* (12), 792–804.
- (23) He, Z. D.; Hanselman, S.; Chen, Y. X.; Koper, M. T. M.; Calle-Vallejo, F. Importance of Solvation for the Accurate Prediction of

Oxygen Reduction Activities of Pt-Based Electrocatalysts. *J. Phys. Chem. Lett.* **2017**, *8* (10), 2243–2246.

(24) He, Z. D.; Wang, J. Y.; Ouyang, B. Design Principle of Carbon-Supported Single-Atom Catalysts - Interplay between d-Orbital Periodicity and Local Hybridization. *Chem. Mater.* **2024**, *36* (3), 1405–1412.

(25) Kim, Y. T.; Lopes, P. P.; Park, S. A.; Lee, A. Y.; Lim, J.; Lee, H.; Back, S.; Jung, Y.; Danilovic, N.; Stamenkovic, V.; et al. Balancing activity, stability and conductivity of nanoporous core-shell iridium/iridium oxide oxygen evolution catalysts. *Nat. Commun.* **2017**, *8* (1), No. 1449.

(26) Zhu, K. Y.; Shi, F.; Zhu, X. F.; Yang, W. S. The roles of oxygen vacancies in electrocatalytic oxygen evolution reaction. *Nano Energy* **2020**, *73*, No. 104761.

(27) Svensson, R.; Gronbeck, H. Dynamics of Dilute Nanoalloy Catalysts. *J. Phys. Chem. Lett.* **2024**, *15* (31), 7885–7891.

(28) Huang, W.; Xu, W. H.; Schwarz, W. H.; Li, J. On the Highest Oxidation States of Metal Elements in MO<sub>4</sub> Molecules (M = Fe, Ru, Os, Hs, Sm, and Pu). *Inorg. Chem.* **2016**, *55* (9), 4616–4625.

(29) Connick, R. E.; Hurley, C. R. Chemistry of Ru(VI), Ru(VII) and Ru(VIII) - Reactions, Oxidation Potentials and Spectra. *J. Am. Chem. Soc.* **1952**, *74* (20), 5012–5015.

(30) Hu, S. X.; Li, W. L.; Lu, J. B.; Bao, J. L.; Yu, H. S.; Truhlar, D. G.; Gibson, J. K.; Marcalo, J.; Zhou, M.; Riedel, S.; et al. On the Upper Limits of Oxidation States in Chemistry. *Angew. Chem., Int. Ed. Engl.* **2018**, *57* (12), 3242–3245.

(31) Riedel, S.; Kaupp, M. The highest oxidation states of the transition metal elements. *Coord. Chem. Rev.* **2009**, *253* (5–6), 606–624.